

A High-resolution Scintillating Fiber Tracker With Silicon Photomultiplier Array Readout

B. Beischer^a, H. Gast^{a,1}, R. Greim^a, W. Karpinski^a, T. Kirn^a, T. Nakada^b,
G. Roper Yearwood^a, S. Schael^a, M. Wlochal^a

^a*I. Physikalisches Institut B, RWTH Aachen University, 52074 Aachen, Germany*

^b*Ecole Polytechnique Fédérale de Lausanne, Dorigny, 1015 Lausanne, Switzerland*

Abstract

We present prototype modules for a tracking detector consisting of multiple layers of 0.25 mm diameter scintillating fibers that are read out by linear arrays of silicon photomultipliers. The module production process is described and measurements of the key properties for both the fibers and the readout devices are shown. Five modules have been subjected to a 12 GeV/ c proton/pion testbeam at CERN. A spatial resolution of 50 μm and light yields exceeding 20 detected photons per minimum ionizing particle have been achieved, at a tracking efficiency of more than 98.5%. Possible techniques for further improvement of the spatial resolution are discussed.

Key words: tracker, scintillating fiber, silicon photomultiplier, SiPM, MPPC

1. Introduction

Scintillating fiber trackers [1] have been realized for a number of experiments such as DØ [2], MICE [3], CHORUS [4] and K2K [5]. Of these, the DØ Central Fiber Tracker has achieved the best resolution of about 0.1 mm using double layers of 0.835 mm thin fibers read out by Visible Light Photon Counters (VLPCs)[6]. VLPCs offer single-photon resolution due to a high internal gain of about 10^4 and are linear up to hundreds of photons. The main drawback of VLPCs is that they have to be operated at cryogenic temperatures which introduces a significant overhead into the operation of scintillating fiber trackers as used in the DØ and MICE experiments. The CHORUS fiber tracker achieves a spatial resolution of 0.185 mm for a single ribbon of 7 layers of 0.5 mm thin scintillating fibers and uses CCD cameras instead of VLPCs for readout, as does the K2K scintillating fiber tracker. CCD cameras require image intensifiers to

¹Present address: Max-Planck-Institut für Kernphysik, Saupfercheckweg 1, 69117 Heidelberg, Germany. Tel.: +49 6221 516-634, Fax: +49 6221 516-603, Email: henning.gast@mpi-hd.mpg.de

detect the few tens of photons that thin scintillating fibers emit for a minimum ionizing particle. Image intensifiers and photomultipliers are sensitive to magnetic fields and require operating voltages of a few thousand volts.

A new type of scintillating fiber tracker has become possible with the advent of silicon photomultipliers [7, 8, 9, 10, 11, 12] (SiPMs) as a viable alternative for the commonly used photon detectors. SiPMs like VLPCs have a high intrinsic gain of $10^5 - 10^6$ but can be operated at room temperature. Furthermore, they are insensitive to magnetic fields and are operated at voltages of 20 V – 80 V. Another key feature of SiPMs are their compact dimensions. This allows the design of detector modules that have almost no dead area if integrated SiPMs are used as photon detectors.

In this article, we describe the design of a new tracking device aiming at the detection of charged particles with an efficiency above 98.5 % and a spatial resolution of 0.05 mm. It consists of modules made of ribbons of 0.25 mm diameter scintillating fibers that are read out by silicon photomultiplier arrays. After an overview of the tracker and module design, the process of module production as well as the optical hybrid used for readout are described in section 2. Sections 3 and 4 deal with the scintillating fibers and silicon photomultiplier arrays employed, respectively. Finally, the performance of several prototype modules as determined in a testbeam at CERN is evaluated in section 5. Possible future improvements are discussed in section 6.

2. Tracker layout

2.1. Tracker and module design

The tracker described here is being developed for use in the PEBS [13] balloon-borne detector. It consists of layers made up from modules like the one depicted in figure 1. Charged particles traversing the module deposit energy in two ribbons of scintillating fibers that are located at the top and bottom of the module, creating scintillation photons. A small fraction of the scintillation light is then guided by total internal reflection to the fiber ends where it is detected by silicon photomultiplier arrays. Each module thus allows two independent measurements of the intersection point of a trajectory. The modules are Z-shaped which allows for them to be placed closely next to each other so that there are no gaps in a tracker layer. The overlap between the modules allows for internal alignment with tracks within one layer. Each module consists of a mechanical support made up from low-density (50 kg/m^3) Rohacell foam between two thin (0.1 mm) carbon fiber skins. It carries scintillating fiber ribbons that are 32 mm wide and up to 2 m long on both sides. A fiber ribbon consists of five layers of 0.25 mm thin scintillating fibers, glued together in the tightest arrangement. Each module end holds two precision pins for a controlled mounting of optical hybrids carrying four SiPM arrays each. The SiPM arrays have a 8 mm wide and 1 mm high active area and are segmented into 32 individual SiPMs with 80 pixels each, with a readout pitch of 0.25 mm, matching the diameter of the fibers. Groups of 32 fiber columns are read out by an SiPM array at alternating

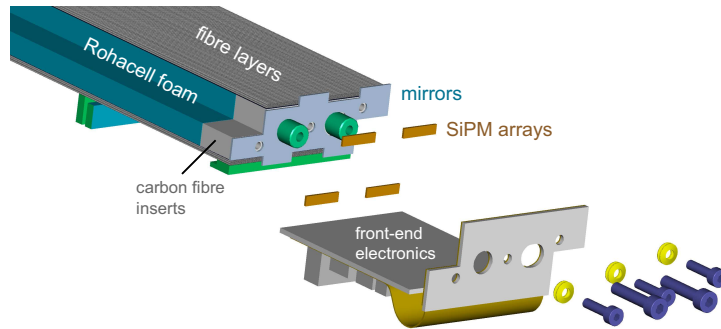


Figure 1: Exploded view of a tracker module. Two ribbons of scintillating fibers located at the top and bottom are carried by Rohacell foam with carbon fiber inserts at the ends. Optical hybrids equipped with silicon photomultiplier arrays and mirrors are screwed to the sides of the module. A corresponding hybrid is mounted to the far side of the module so that each fiber is covered by an SiPM channel on one side and a mirror on the other. The large screws will be used to mount the module to the tracker walls.

ends of the module. Due to the mounting of the SiPM arrays, sensors cannot be placed next to each other without a dead area of 0.25 mm between them. To minimize this dead zone, a mirror covers the space between the SiPMs in order to increase the light collection on the opposite fiber end.

2.2. Module production

Kuraray SCSF-81MJ fibers [14] (sec. 3) with a diameter of 0.25 mm are used for the tracker modules. Ribbons of five layers of 128 fibers each are produced in a winding process similar to the one used to produce the fiber trackers for the CHORUS and K2K experiments. The scintillating fiber arrives uncut on a spool from the manufacturer. A helical groove with a pitch of 0.275 mm, to accommodate small variations in the fiber thickness, is cut into an aluminum drum of 200 mm diameter on a winding machine. The diameter is a free parameter and can be adapted to the required module length. A release agent is applied to the drum prior to the ribbon production. One layer of scintillating fiber is then wound on top of the drum, with its position precisely fixed by the helical groove, using a controlled tension of 20 g and EpoTek 301M is applied as an adhesive. The fiber end is fixed with a fast curing adhesive and cut. The next fiber layer is wound on top of the first layer so that the fiber lies in the gap between fibers of the previous layer maintaining a constant fiber pitch over the layers. This process is repeated applying an adhesive to the fibers after each completed layer until five layers of fibers have been wound on top of the drum. After the last fiber layer has been completed, two aluminum end-pieces are screwed next to each other onto the drum to ease the handling of the fiber ribbon. The drum continues to rotate at a constant speed for a few hours until the adhesive is cured. The ambient temperature for the whole process is kept at 22 °C. The fiber ribbon is then cut between the end-pieces, taken off the drum and placed in a Teflon bed that is filled up with glue and then covered

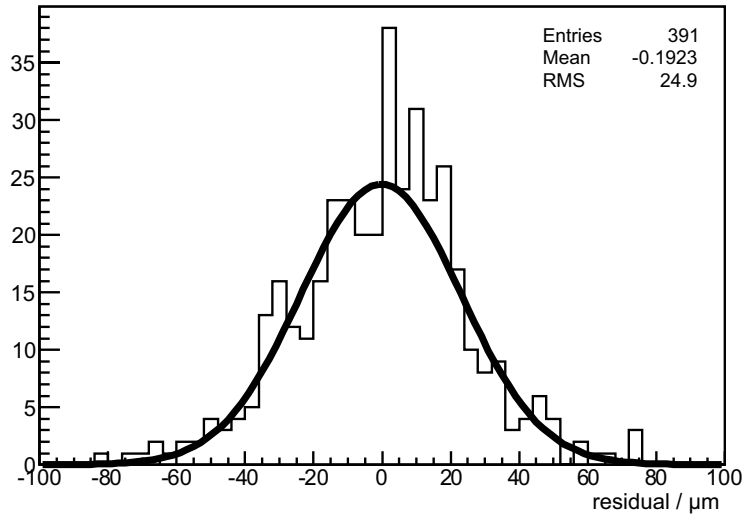


Figure 2: Distribution of the deviation of the fiber centers from a uniform lattice with a pitch of 0.275 mm, shown here for the fibers included in the picture of fig. 3. The black line is a Gaussian fit to the data, plotted here for illustrative purposes.

by a glass plate. After the glue has fully cured, the setup with the fiber ribbon is placed in an oven heated to approximately 50 °C to allow the fiber ribbon to straighten out.

The precision of the fiber placement in the ribbons is determined by scanning the cross-section in the end-pieces to be better than 0.025 mm for a ribbon consisting of 5 layers of about 128 fibers each (fig. 2). A photograph of the front of a completed ribbon, illuminated from above, is shown in figure 3.

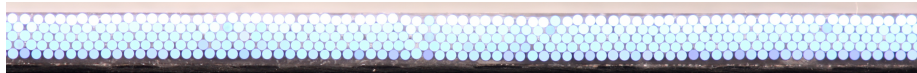


Figure 3: Close-up photograph of a completed fiber ribbon made of Kuraray SCSF-81MJ fibers of 0.25 mm diameter. The nominal gap in the horizontal direction is 0.025 mm. Five layers of fibers are placed in the tightest arrangement. The supporting carbon fiber skin is seen at the bottom of the picture.

Two fiber ribbons are glued to the top and bottom of a mechanical support made from a 10 mm thick Rohacell foam layer contained between two 0.1 mm thin carbon fiber skins. Polycarbonate end-pieces are embedded in the support structure to allow the mounting of the optical hybrid. The module ends are then polished to achieve a good optical coupling between the fibers and the SiPMs. Finally, optical readout hybrids carrying the SiPMs (sec. 2.3) on a PCB board including the mirrors are screwed directly to the polished fiber ends on both sides of the module.

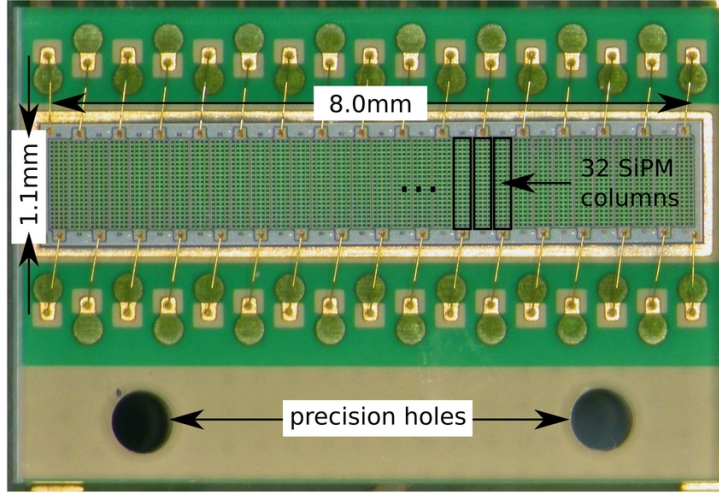


Figure 4: Microscope picture of a Hamamatsu MPPC 5883 SiPM array containing 32 individual SiPMs with a pitch of 0.25 mm. The active area of each SiPM measures 1.1 mm in height. The individual SiPMs are bonded towards alternating sides. Each SiPM contains 80 pixels that are organized in 20 rows and four columns.

2.3. Optical hybrid and data acquisition

The fiber modules are read out by SiPM arrays of type Hamamatsu MPPC 5883 (fig. 4). Each array consists of 32 independent SiPMs (called channels in the following) and is mounted to a ceramic and protected by an epoxy layer above the sensitive area of the semiconductor. The detector signals are read out by bonding wires that are fed through to the backside of the ceramic. Section 4 deals with a detailed performance study of the SiPM arrays.

Four arrays are positioned on an optical hybrid (fig. 5) in the following way: The detectors are glued to a printed circuit board in a mechanical device for placing the detectors with an accuracy of $10\ \mu\text{m}$. The device is a flat surface equipped with four groups of two neighboring positioning pins for placing the SiPM arrays in the geometry defined by the tracker module. The SiPM arrays are pinned up in their precision holes face down. A shadow mask with holes at the position of the contacts is put inside the device to brush a conductive glue of type Elecolit 323 into the holes and thus on the contacts. After the mask has been removed, the PCB is pressed on the contacts with a defined pressure. After this procedure, mirrors are placed inside the gap between the SiPM arrays to increase the light yield at the opposite side of a fiber module. Two completed hybrids are screwed to the sides of a fiber module. The hybrid is read out by a specially developed front-end electronics board based on VA_32/75 chips produced by IDEAS, Norway [15]. VA_32/75 chips are charge sensitive preamplifiers with a sample and hold stage. They have 32 channels each with a shaping time of 75 ns and a linear range of 36 fC [15]. Due to the gain of

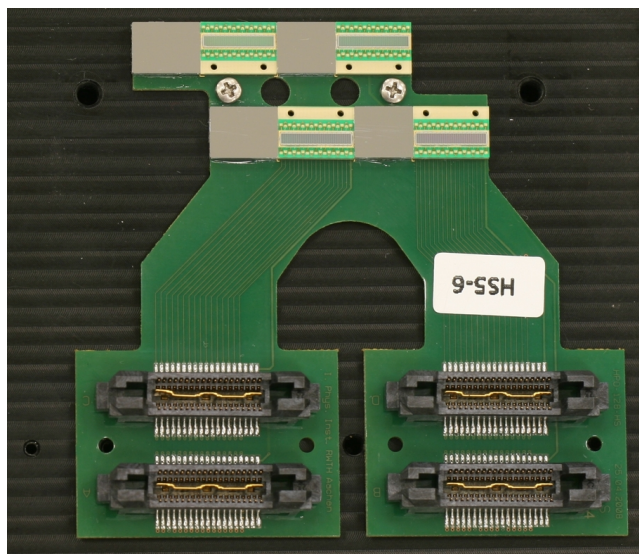


Figure 5: Optical hybrid. Four SiPM arrays with mirrors in between are visible at the top of the picture, together with the connectors to the front-end electronics in the lower part.

$\sim 10^6$ of SiPMs the signals have to be attenuated in a resistor network on the front-end board by a factor of 150 to match the dynamic range of the chip.

An external trigger generates a hold signal for the VA chips on the front-end board with a delay of the shaping time of the preamplifier, so that the SiPM signals are sampled and their amplitudes stored on the VA_32/75 chips for readout. The stored analog signal heights are digitized sequentially by 12 bit 5 MHz sampling ADCs on back-end boards. The data are subsequently transferred to a PC via a QuickUSB interface produced by Bitwise Systems [16].

3. Scintillating fibers

Kuraray SCSF-81MJ fibers were chosen for the tracker because their peak emission wavelength at 437 nm matches the peak sensitivity of the employed SiPMs. The fibers are multicladd, consisting of a scintillating fiber core with a refractive index of 1.59 surrounded by two claddings with refractive indexes of 1.49 and 1.42, respectively, which are approximately $10 \mu\text{m}$ thin. Measurements of the key properties of the fibers are shown in the following: A long attenuation length and uniform thickness are vital for use in a large-area tracking device, while the angular emission spectrum is needed for an understanding of the observed spatial resolution.

3.1. Attenuation length

The manufacturer specifies an attenuation length of at least 3.5 m. We conducted a separate measurement of the attenuation length for four 5 m long

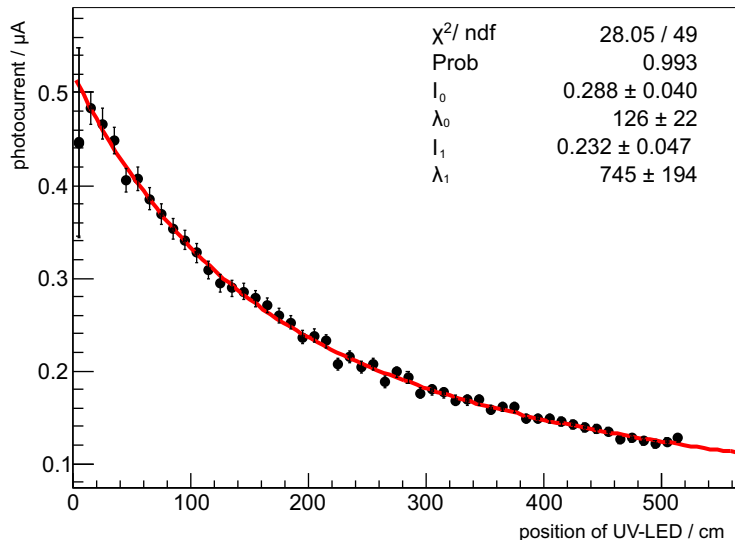


Figure 6: Determination of the absorption length of the scintillating fibers. The mean photocurrent measured for four approximately 5 m long samples of fiber is shown. A UV-LED has been used to excite the fibers. The curve is a fit according to eq. (1), and the fit parameters are given in the inset.

samples of Kuraray fibers. A UV-LED was used to excite the fiber locally while a photo-diode was used to measure the photo-current I as a function of position x of the UV-LED (fig. 6). A two-component exponential function

$$I(x) = I_0 \exp(-x/\lambda_0) + I_1 \exp(-x/\lambda_1) \quad (1)$$

was fitted to the measured photo-current. The result shows that the light trapped within the fiber is made up of two components of roughly equal intensity. The first component has a short attenuation length of roughly $\lambda_0 = (1.3 \pm 0.2)$ m while the second component shows a longer attenuation length of $\lambda_1 = (7.5 \pm 2)$ m. The mean attenuation length over the first two meters of fiber, obtained from a fit to a single exponential, is approximately (2.6 ± 0.1) m. This is the figure that limits the module length.

3.2. Thickness measurements

The thickness of the fiber was controlled by the manufacturer using a micrometer on two 15 m long samples finding a mean thickness of 0.252 mm and a root mean square variation of 0.009 mm. The fiber is also measured prior to assembly by a calibrated Zumbach ODAC-XY [17] laser micrometer. The result of the measurement is shown in figure 7. The fiber diameter of (0.255 ± 0.009) mm is in good agreement with the measurement from Kuraray. Furthermore, the simultaneous measurement in two directions allows to study the ellipticity of the fiber and no deviation from a circular shape was detected.

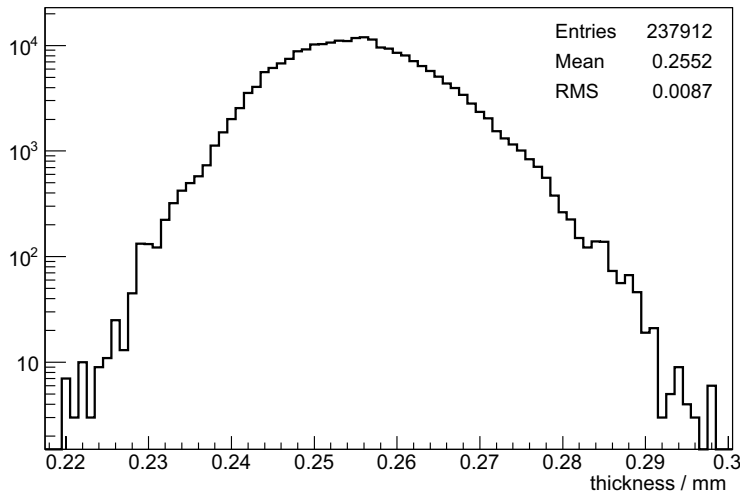


Figure 7: Quality assurance of the scintillating fibers. The thickness of the Kuraray SCSF-81MJ fibers used in the module production process have continuously been sampled over 3 km of fiber. The nominal pitch of 0.275 mm accommodates the small variations in fiber thickness.

3.3. Angular emission spectra

The angular emission spectrum of the fiber has been measured using a Hamamatsu LEPAS optical beam measurement system [18]. The setup records an image of the light emitted from the fiber end and uses it to calculate the far-field. As its angular range is limited to $\pm 41^\circ$, part of the cladding modes, which are trapped in the fiber by the outer cladding, and helix modes, which are emitted from the fiber end under a large angle of emission, could not be measured. The result is shown in figure 8. It is compared to the prediction of a Monte Carlo simulation based on Geant4 [19] that traces the trajectories of optical photons, based on an idealized cylindrical fiber geometry, refractive indexes and absorption using geometric optics. As shown in the figure, the simulation is in agreement with the far-field measurement over the most part of the accessible angular range and predicts an average angle of emission of about 35° with respect to the fiber axis in a medium matching the refractive index of the fiber core. The features at 35° and 46° in the Geant4 simulation show the transitions from core modes trapped within the fiber core to cladding modes that are totally reflected by the outer cladding and from cladding modes to helix modes that are trapped in the fiber region very close to the fiber claddings, respectively. The implication for the tracker module design is that the silicon photomultipliers have to be mounted as close to the fiber ends as technically possible. Any gap, for example from an protective epoxy layer on top of the SiPM, significantly smears out the position information carried by the photons. In this case photons emitted from a fiber will not necessarily be detected by the SiPM array channels directly in front of that fiber. As a consequence, the spatial resolution deteriorates.

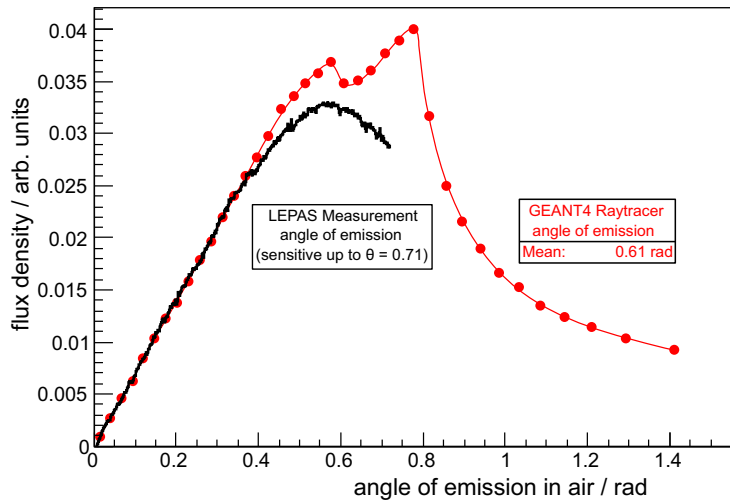


Figure 8: The angular distribution of photons emitted from the fiber shows that the photons exit the fiber under an average angle of 0.61 rad (35°) with respect to the fiber axis.

4. Silicon photomultiplier arrays

A silicon photomultiplier (SiPM) [7, 8, 9, 10, 11, 12] is a novel solid state photo-detector. In principle, it consists of a matrix of avalanche photo diodes (APDs) that are operated in Geiger mode, i.e. above the breakdown voltage, and can be triggered by an incident photon. The single matrix elements are called pixels and the output signal is then proportional to the number of pixels that have fired. This will in turn be proportional to the number of incident photons as long as this number is small compared to the number of pixels. The mode of operation leads to a high intrinsic gain of the SiPM on the order of 10^5 to 10^6 . They have the virtues of high quantum efficiency, as well as compactness, auto-calibration, and insensitivity to magnetic fields. This allows for them to be used inside a particle spectrometer. The Hamamatsu MPPC 5883 SiPM arrays used for the tracker consist of 32 independent SiPMs ("channels") with a pitch of 0.25 mm. Each channel has 4×20 pixels providing enough dynamic range for minimum ionizing particles (MIPs) of charge $z \lesssim 4$ in the tracker, given that a singly-charged MIP will trigger typically 10 pixels per channel (sec. 5.3). At high light yields, saturation effects due to the limited number of pixels will lead to a departure from the linearity between the number of triggered pixels and the number of incident photons.

The key figure of merit of an SiPM is its photon detection efficiency ϵ_{PDE} which can be expressed as the product

$$\epsilon_{\text{PDE}} = \epsilon_{\text{ABE}} \cdot \epsilon_{\text{QE}} \cdot \epsilon_{\text{FF}} \quad (2)$$

where ϵ_{ABE} denotes the avalanche breakdown efficiency, ϵ_{QE} the quantum efficiency of the pixels and ϵ_{FF} the fill factor that depends on the geometry of the

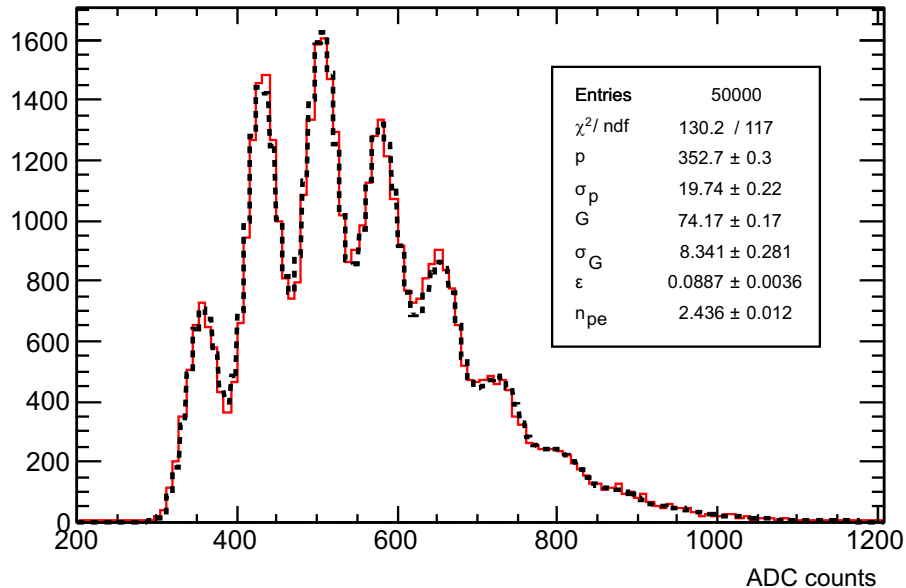


Figure 9: An LED spectrum of a Hamamatsu MPPC 5883 (solid line) together with the fitted model curve (dashed line) used for the determination of the calibration parameters (sec. 4.1).

SiPM and is the critical factor in the determination of ϵ_{PDE} . In the following, the method used for the SiPM calibration is briefly reviewed in section 4.1. Measurements of the fill factor and the photon detection efficiency are described in sections 4.2 and 4.3, respectively. For a reliable operation of the tracker, the homogeneity of the response of individual array channels is crucial and this is explored in sec. 4.4. Photons produced in the avalanche process can cause neighboring pixels to fire. This crosstalk effect is a potential obstacle in the operation of SiPMs. The determination of the crosstalk probability is therefore the topic of sec. 4.5.

4.1. Analysis of LED spectra

The measurements of the photon detection efficiency, homogeneity, and crosstalk presented here rely on the analysis of LED spectra (fig. 9) which are fitted with the model of Balagura et al. as described in [20]. In this model, the five free parameters characterizing the SiPM are the pedestal position p , the pedestal width σ_p , the gain G , the signal width σ_G describing the spread of signals from different pixels, and the pixel crosstalk probability ϵ (sec. 4.5). In addition, the shape of the spectrum depends on the mean number of photo-electrons n_{pe} . An example of the fit is given in figure 9. The width of the n -th photo-electron peak is approximately given by $\sigma_n = \sqrt{n\sigma_G^2 + \sigma_p^2}$ so that only

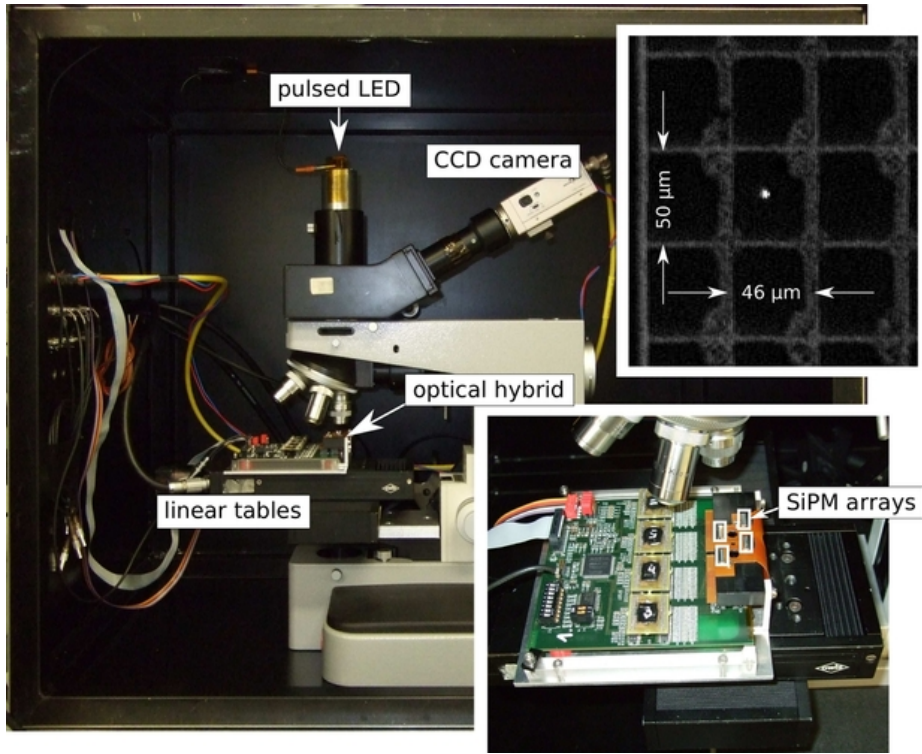


Figure 10: Setup to determine the fill factor of SiPMs. *Top right:* Close-up view of the LED focus achieved. The size of the focus should be compared to the size of the SiPM pixels visible in the background. *Bottom right:* Close-up view of an optical hybrid equipped with four SiPM arrays, together with readout electronics, in the object plane of the microscope.

the first few photo-electron peaks can usually be resolved. Here, the gain is simply the spacing between two photo-electron peaks, measured in ADC counts. Pixel crosstalk leads to a deviation from the underlying Poissonian shape.

4.2. Fill factor

The ratio of sensitive to total area of an SiPM is called geometric efficiency or fill factor ϵ_{FF} . A setup to determine ϵ_{FF} has been built in Aachen (fig. 10). It consists of a commercial microscope in which an LED is mounted behind a small pinhole. Using the light path of the microscope, the spot is focused down to less than $5 \mu\text{m}$. The object plane can be moved two-dimensionally with high precision linear tables using computer-controlled stepper motors.

To determine ϵ_{FF} , an SiPM is mounted on the linear tables. The surface is scanned in both directions and the surface of the SiPM is illuminated by a series of 5 ns short LED flashes. We define that a point at which a pixel fires at least 95% of the time belongs to the sensitive area. For the determination

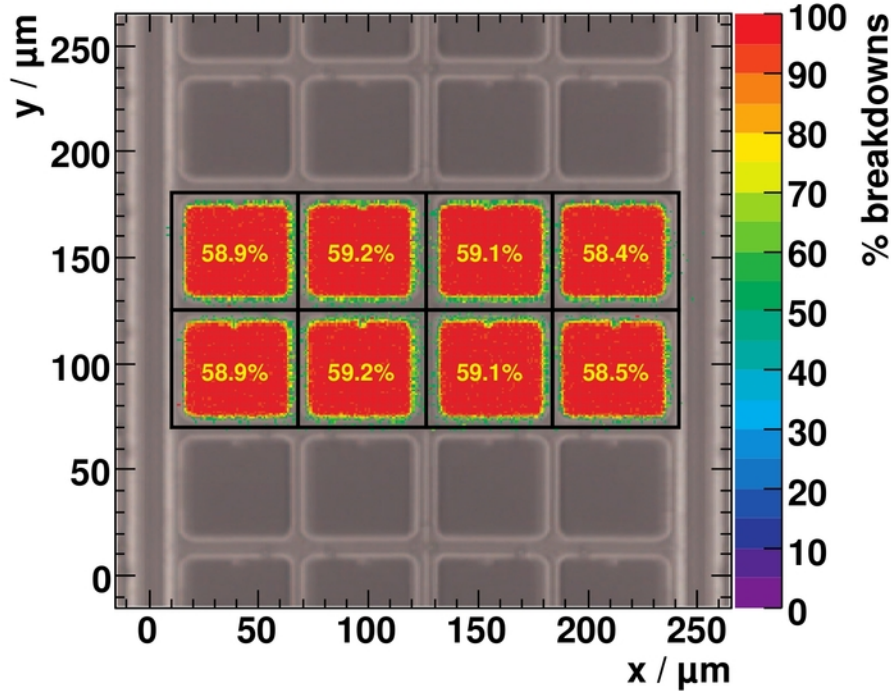


Figure 11: Determination of the fill factor for eight pixels of an MPPC 5883, using an extremely fine grid of sampling points with the microscope setup shown in fig. 10. A microscope picture of the SiPM surface is shown in the background. The scale gives the percentage of breakdowns triggered at each scan position.

of the fill factor, a very fine grid of $1\ \mu\text{m}$ spacing is used. By using a coarser scanning grid, SiPM arrays can routinely and quickly be tested for dead pixels before assembly of the optical hybrids.

In fig. 11, the fill factor of eight pixels of an Hamamatsu MPPC 5883 array is plotted as an example, together with a microscope picture of the device. Averaging over the individual pixels yields a mean pixel fill factor of $\epsilon_{\text{FF}}^{\text{pix}} = 59.4\%$. In the determination of the overall photon detection efficiency however, the gaps between neighboring SiPM channels have to be taken into account, and the fill factor, averaged over the channel width of $250\ \mu\text{m}$, then becomes $\epsilon_{\text{FF}} = 55.2\%$.

4.3. Photon Detection Efficiency

The photon detection efficiency ϵ_{PDE} is measured by shooting LED flashes onto an SiPM and comparing the mean number of detected photons to those of a calibrated photomultiplier tube with known quantum efficiency ϵ_{PMT} . Considering the sensitive areas A_{PMT} and A_{SiPM} , as well as the mean number of

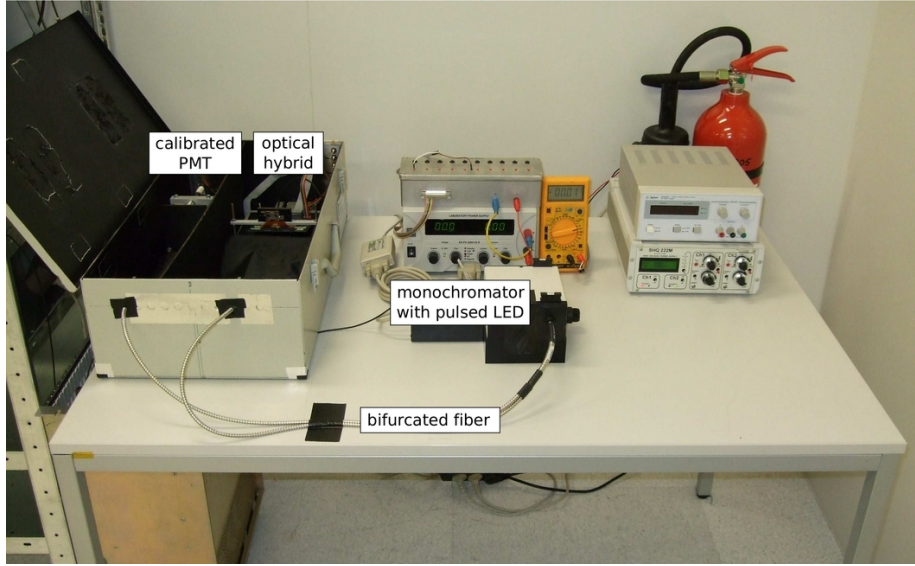


Figure 12: Setup to measure the photon detection efficiency of the SiPMs.

photo-electrons \bar{n}_{PMT} and \bar{n}_{SiPM} of the PMT and SiPM, respectively, the photon detection efficiency can be determined from

$$\frac{\bar{n}_{\text{PMT}}}{\epsilon_{\text{PMT}} \cdot A_{\text{PMT}}} = \frac{\bar{n}_{\text{SiPM}}}{\epsilon_{\text{PDE}} \cdot A_{\text{SiPM}}} \quad (3)$$

In the test setup (fig. 12), the LED is flashed into a monochromator. Its light is then split by a calibrated 50/50 bifurcated fiber and guided to two optically separated sections of a light-tight box. The calibrated PMT and the optical hybrid are placed at the same distance of 30 cm. A diffusor is used to guarantee that the SiPM and the PMT are illuminated uniformly. The response of the PMT is measured with a charge-to-digital converter. The same model used to fit the SiPM spectra is employed to determine the mean number of photo-electrons in the PMT by setting the pixel crosstalk probability to zero.

ϵ_{PDE} is measured as a function of the bias voltage U applied to the SiPM between 70.0 V and 71.75 V in 0.25 V steps. The power supply can be controlled from a lab PC, such that the whole characterization is fully automatic. All measurements have been performed at a temperature of $T = 20^\circ\text{C}$.

The photon detection efficiency depends on the overvoltage at which the SiPM is operated, defined as $\Delta U = U - U_0$ where U_0 is the breakdown voltage of the SiPM. U_0 is determined by measuring the gain G as a function of the bias voltage, at bias voltages $U > U_0$. The resulting linear curve can then be extrapolated down to zero gain and the corresponding voltage is U_0 .

In fig. 13 (left), the mean photon detection efficiency of 1441 channels of Hamamatsu MPPC 5883 devices is plotted as a function of the mean overvoltage

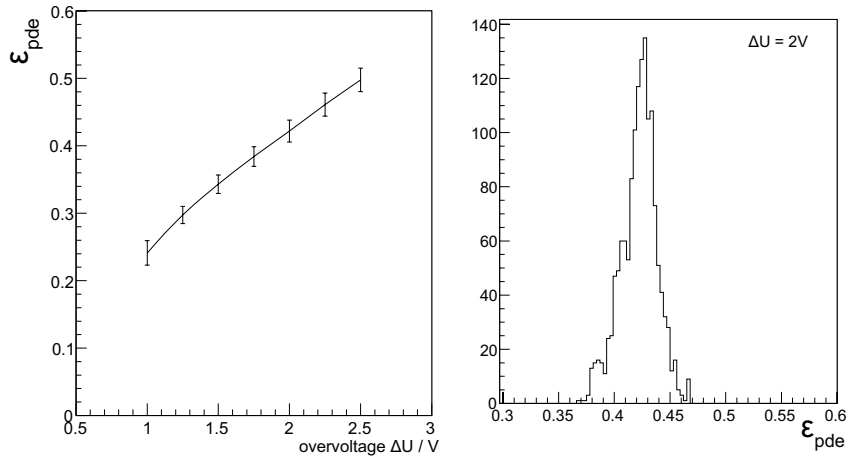


Figure 13: Mean photon detection efficiency of 1441 channels of Hamamatsu MPPC 5883 devices as a function of the overvoltage at a wavelength of $\lambda = 440 \text{ nm}$. The line has been added to guide the eye (left). Photon detection efficiency distribution of 1441 channels on 46 SiPM arrays at a mean overvoltage of 2.0 V (right).

$\overline{\Delta U} = U - \bar{U}_0$, at a fixed wavelength of $\lambda = 440 \text{ nm}$. The error bars indicate the standard deviation of Gaussians fitted to the distribution of each point. Here, \bar{U}_0 is the mean breakdown voltage of the respective array. As an example of the individual distributions, figure 13 (right) contains the values determined for ϵ_{PDE} at an overvoltage of $\overline{\Delta U} = 2.0 \text{ V}$, for 1441 channels on 46 arrays. 31 channels did not work because of broken electrical contacts. This problem has been solved for the testbeam measurements by changing the connection technique from gluing to soldering. The channel-to-channel variation is found to be at the level of a few percent, comparable to the variation in breakdown voltage (sec. 4.4).

ϵ_{PDE} reaches a level of 50% at an overvoltage of 2.8 V. This result underlines that the silicon photomultiplier has reached a level of maturity where its photon detection efficiency is mainly determined by its geometrical properties, expressed in terms of the fill factor, as comparison with eq. (2) shows that the product $\epsilon_{\text{ABE}} \cdot \epsilon_{\text{QE}}$ must be close to unity. Nevertheless, care must be taken when determining the optimal voltage at which to operate the SiPMs in the tracker. This is because pixel and strip crosstalk increase along with ΔU , deteriorating the spatial information and thereby counteracting the beneficial effect of the increased light yield.

In fig. 14, the spectral response of the devices can be seen for four overvoltages between 1 V and 2.8 V. The peak sensitivity is reached at a wavelength of 460 nm matching the peak emission wavelength of Kuraray SCSF-81MJ scintillating fibers.

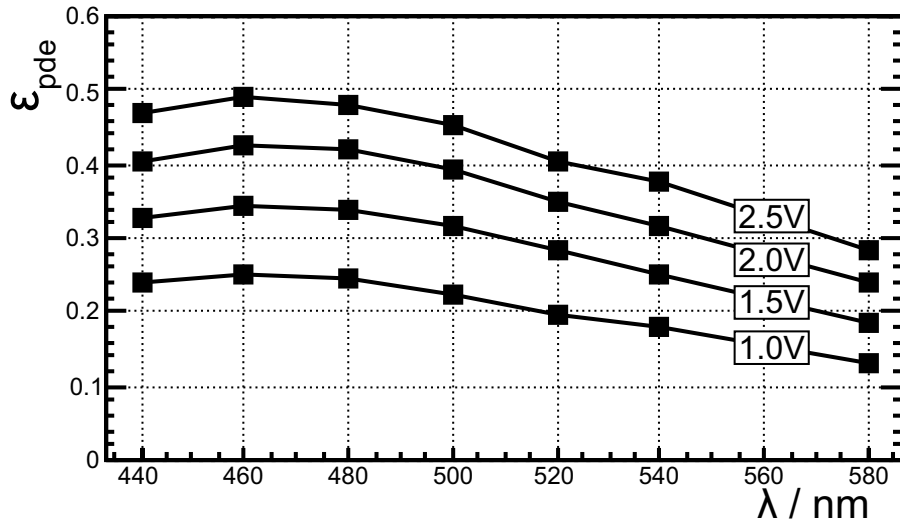


Figure 14: Spectral response of a Hamamatsu MPPC 5883 for four overvoltages between 1 V and 2.5 V. The photon detection efficiency peaks at $\lambda = 460$ nm. Lines have been added to guide the eye.

4.4. Homogeneity

To study the homogeneity of the SiPMs, the breakdown voltages of 1441 channels on all 46 Hamamatsu MPPC 5883 arrays available in Aachen have been determined (fig. 15 (left)). While the breakdown voltage varies by around 2 V, we find an RMS variation of the breakdown voltage from channel to channel of only 0.037 V. This is illustrated in fig. 15 (right) showing the distribution of $U_0 - \bar{U}_0$. The breakdown voltages of the first channels in the arrays scatter by a much larger amount. The cause for this effect is currently under investigation.

The homogeneity of the gain is demonstrated in figure 16 showing LED spectra taken with a typical Hamamatsu MPPC 5883. The response of each of the 32 channels, operated at the same bias voltage, is shown after shifting the pedestal to the same value of 300 ADC counts. The individual photo peaks are visible, illustrating the auto-calibration capability of the SiPM. The gain G is related to the distance between two peaks and is clearly seen to be homogeneous over the entire array.

To summarize our findings, the key properties gain and photon detection efficiency were found to be nearly identical at a fixed temperature for all SiPM channels of all examined arrays as long as they are operated at the same overvoltage. For a reliable operation of the tracker, ΔU therefore needs to be kept constant at an optimal value, and it has to be adjusted separately for each array, but not for each channel, which greatly simplifies the operation.

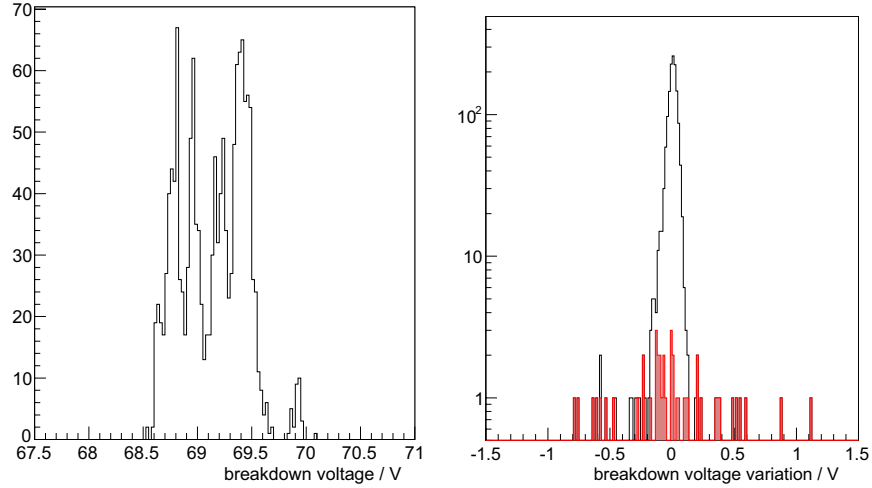


Figure 15: Distribution of the breakdown voltage U_0 of 1441 channels of Hamamatsu MPPC 5883 devices (left). After subtraction of the mean breakdown voltage of the corresponding array, the small channel-to-channel variation remains (right, unshaded histogram). The distribution obtained for the first channel in each array (shaded histogram) shows a larger variation.

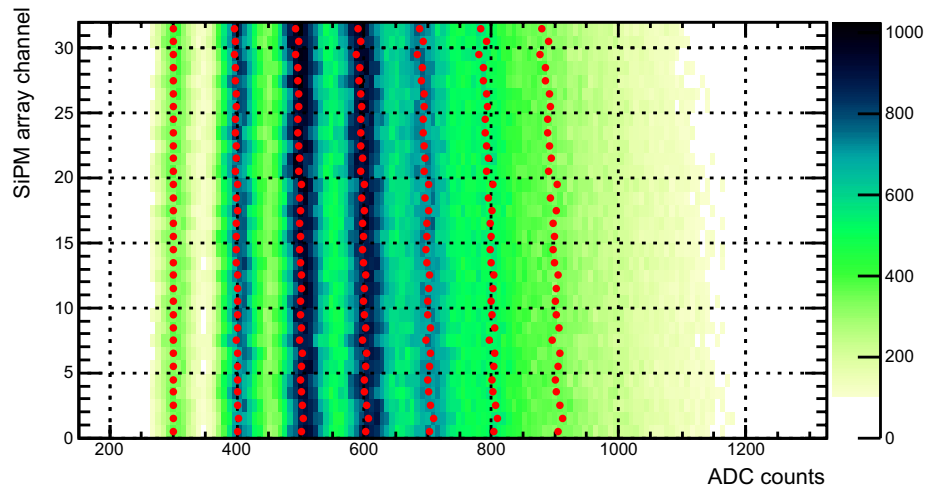


Figure 16: To study the homogeneity of the SiPM response, LED spectra of the Hamamatsu MPPC 5883 devices are measured. Each bin along the y -axis corresponds to one SiPM in the array. The pedestal values have been equalized for better comparison of the gain values. The dots mark the positions of the first few photo-electron peaks.

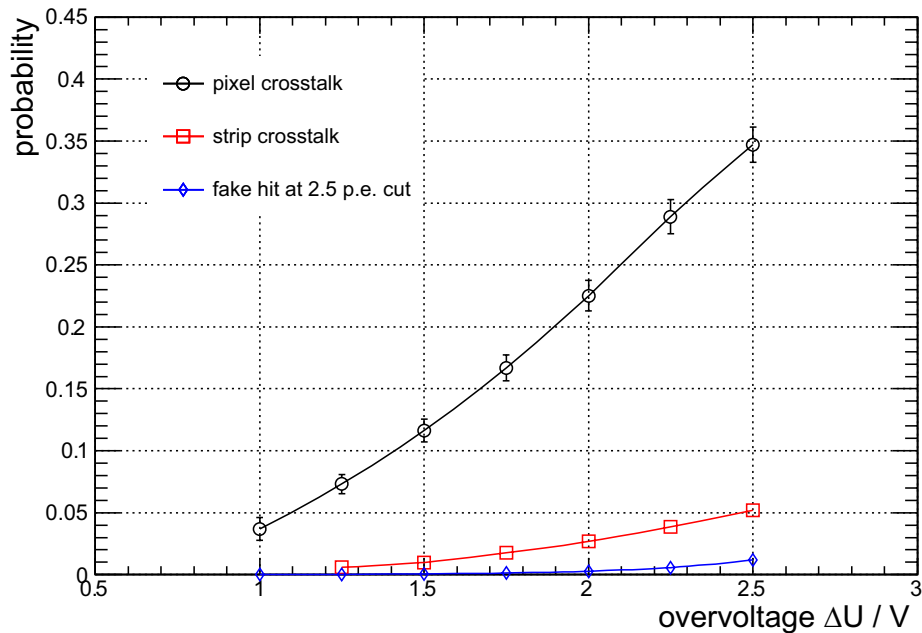


Figure 17: Pixel crosstalk, strip crosstalk and fake hit probability of the SiPM arrays as a function of the overvoltage. Lines have been added to guide the eye.

4.5. Crosstalk and noise

When an avalanche develops in a given pixel, photons are produced that can subsequently trigger a neighboring pixel. This effect is known as pixel crosstalk [21] and the probability for a pixel to trigger a neighboring pixel is called the crosstalk probability ϵ . It can be measured from the same LED spectra used for the determination of the photon detection efficiency, as described in the beginning of this section. Figure 17 shows the pixel crosstalk probability as a function of the overvoltage. Each point shows the mean value of the examined sample and the error bars give the root mean square variation across the sample.

Worse than pixel crosstalk, photons from the avalanche process can reach neighboring array strips and cause them to fire. This effect is called strip crosstalk. The strip crosstalk probability ϵ_s is defined as the probability for any of the neighboring channels to be triggered by an SiPM breakdown. It can be determined from noise measurements by looking at coincidences of fired channels and correcting for random coincidences. ϵ_s is found to be lower than ϵ by roughly an order of magnitude (fig. 17). The crosstalk probabilities measured constitute a major problem in the operation of the SiPM arrays, and these results provide key input to Monte Carlo studies used to determine the ideal operating point in terms of the overvoltage.

When operated above U_0 , SiPM pixels fire randomly due to thermal generation of charge carriers, thus creating a fake hit in the tracker module. Dark

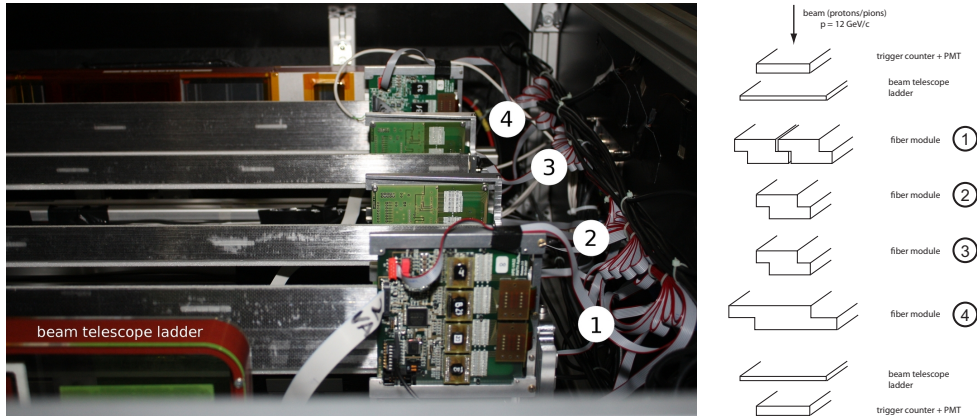


Figure 18: A perspective photograph (left) and schematic drawing (right) of the 2009 testbeam setup. The five modules studied in the testbeam are visible: two narrow modules (128 fibers wide, (2) and (3), fig. 19), one wide module (256 fibers wide, (4), and two narrow modules mounted next to each other (1), with the aim of studying the small gap between the modules. The mounting frames of the silicon beam telescope ladders are visible in front of and behind the four layers of fiber modules, respectively. The overall dimensions of the testbeam box were $120 \times 120 \text{ cm}^2$.

spectra have been taken along with the LED spectra. The gain can be determined from the LED spectra and thus a 2.5 photo-electron threshold can be applied to the noise spectra from which the corresponding fake hit probability per array strip can be determined (fig. 17). At $T = 20^\circ\text{C}$, a probability of 0.3% is reached at 2.0 V overvoltage. A scintillating fiber tracker for use in particle or astroparticle physics will typically consist of $\mathcal{O}(4 - 12)$ layers of fiber modules. Track finding algorithms to identify the hits belonging to a particle trajectory in the presence of fake hits have been implemented [22] that can easily cope with this kind of noise level.

5. Testbeam measurements 2009

5.1. Setup description

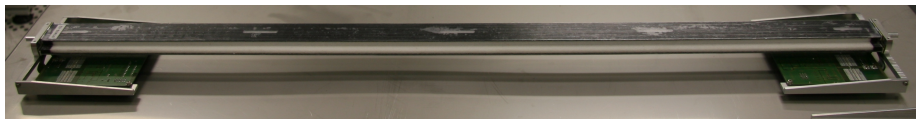


Figure 19: Photograph of a completed narrow module used in the testbeam. Two boards carrying front-end electronics are visible at the sides.

Five 860 mm long prototype modules for the fiber tracker have been subjected to a testbeam at the CERN T9 beam-line in fall 2009. The beam consisted

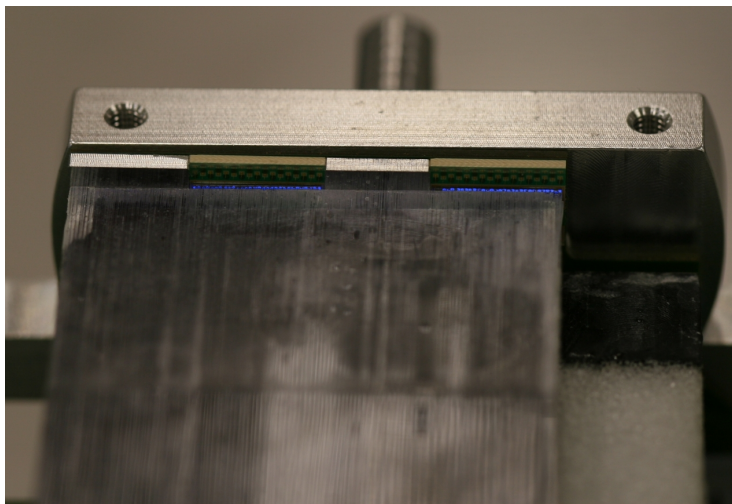


Figure 20: Detailed view of the mounting of a hybrid carrying a silicon photomultiplier array between the end of a fiber ribbon and an aluminum carrier piece. Two mirrors are visible next to two SiPM arrays.

mainly of pions and protons and had a defined momentum of $p = 12 \text{ GeV}/c$. The main goals were the determination of the spatial resolution and of the light yield of the modules.

The testbeam setup (figs. 18, 19, and 20) consisted of two trigger scintillator counters of dimension $20 \times 10 \times 1 \text{ cm}^3$, two double-sided silicon-strip detectors built for the AMS-02 tracker [23] and the five fiber module prototypes that were arranged in four layers (cf. fig. 18). To enable comparison studies, four of the five fiber modules were made of Kuraray SCSF-78MJ fibers while the remaining one was made of SCSF-81MJ fibers. The SCSF-78MJ fibers became available just in time for the testbeam. In addition, for three optical hybrids (12 SiPM arrays), optical grease of type NyoGel OCK-451 or OC-459 [24] was applied to the fiber-SiPM interface. As the beam spot size (rms width) was only about 8 mm in each direction, not all SiPM arrays were illuminated and could be included in the study.

The silicon-strip detectors were used as a beam telescope, allowing a reference measurement of the trajectory of a beam particle which is vital for the determination of the spatial resolution. Under ideal conditions, the beam telescope ladders themselves each provide a spatial resolution of approximately $10 \mu\text{m}$ and $30 \mu\text{m}$ in the coordinates perpendicular and parallel to the fiber axis, respectively [25]. The corresponding readout pitch is $110 \mu\text{m}$ and $208 \mu\text{m}$ for the strips parallel and perpendicular to the fibers, respectively. The trigger scintillators were connected to ordinary PMTs. For the readout of the SiPM arrays, two different preliminary electrical hybrid boards were available, one based on the IDEAS VA.32/75 readout chip [15] and the other based on the

SPIROC [26] readout chip, specifically designed for the readout of SiPMs, with 32 channels each. The temperature at which the SiPMs were operated varied between 22°C and 25°C depending on location in the setup and the day-night cycle. However, thanks to the excellent properties of the used SiPMs, noise did not pose a problem even at these high temperatures.

The trigger scheme was based on NIM electronics and had to be optimized for speed as the hold signal for the VA_32/75 and SPIROC chips reading out the SiPMs had to arrive around 85 ns after the particle crossing as the SiPM signal pulse reaches its maximum at that time. This was achieved by using only a single coincidence of the two PMTs reading out the trigger scintillators. A post-event dead-time of 150 μ s was started along with the hold signal, and a pre-event dead-time of 5 μ s was started by a signal from any of the trigger PMTs. Upon arrival of a trigger signal, the raw data (ADC counts) of all readout channels present in the setup were stored on disk for offline analysis.

The coordinate system was chosen such that the beam traversed the setup in the z -direction, the fibers were parallel to the y -direction and therefore the fiber modules measured the x -direction of a particle track. The double-sided silicon beam telescope modules measured both in the x - and y -directions.

5.2. Analysis procedure

The analysis procedure begins with the calibration of the silicon beam telescope ladders and the SiPM arrays in front of the fiber modules. For this purpose, dedicated calibration runs were taken between spills, before each data run. In a first step, dark events were taken. For the ladders, the pedestal and noise for each strip are determined as the mean and root mean square of the distribution of raw ADC counts. For the SiPM arrays, the pedestals for all channels are determined accordingly. In the second step, LEDs located next to each fiber module were pulsed with a pulse length of 6 ns and the SiPM parameters, especially gain and crosstalk, are determined from fits to the spectra, as described in sec. 4.1. Here, the uniformity of the SiPM response across an array, as demonstrated above, is exploited to speed up the calculations by fitting only the averaged spectrum.

Using the calibration parameters so obtained, clusters can be identified – neighboring channels with amplitudes significantly above the background caused by noise. For the beam telescope ladders, a seed cluster is formed when a strip with a significance exceeding 5σ is found. Neighboring strips are added to the cluster as long as their significance is at least 2σ . If no neighboring cluster fulfilling this condition is found, the one with the highest significance is added nevertheless, in order to make use of the charge-sharing between adjacent strips which improves the spatial resolution [27].

For the SiPM arrays, the raw SiPM data has to be converted to the number of fired pixels. With the pedestal position p_i for a given SiPM channel i and the gain g , as determined during the calibration and constant across an array, the number of pixels s_i for a given channel is then simply calculated from the raw

ADC amplitude a_i according to

$$s_i = \frac{a_i - p_i}{g} \quad (4)$$

Then, fiber clusters are identified, as the photon output of the scintillating fibers for a single minimum ionizing particle is spread over several neighboring SiPM array channels. Starting from a channel with at least 2.5 photo-electrons, neighboring channels are added to the cluster as long as their amplitude exceeds 0.5 photo-electrons. The position of the fiber cluster is then calculated as

$$x_{\text{cl}} = \frac{\sum_i s_i x_i}{\sum_i s_i} \quad (5)$$

where the sum is taken only over the channel with the highest amplitude and its immediate neighbors at most. We found that this prescription slightly improves the spatial resolution.

Each cluster constitutes a potential intersection point of a particle track. In the next step of the analysis chain, we therefore identify straight line tracks, using an algorithm that is based loosely on the Hough transform as implemented in [28]. It exploits the fact that each pair of clusters belonging to the same track will yield similar values for the slope and intercept of the line traversing the two clusters. To determine the track parameters, we perform two simple straight line fits in the xz - and yz -planes, respectively.

Using the tracks and clusters of the complete event sample, we then performed a detector alignment using the Millepede code [29]. We allowed for deviations of the positions of all the SiPM arrays from the nominal ones in the x -direction. The Millepede algorithm minimizes the global χ^2 between tracks and clusters and yields unbiased alignment parameters which we then used for a second iteration of the analysis. We note that possible tilt angles of the fiber modules with respect to each other and the beam telescope modules can be neglected because of the small beam spot size and a mounting precision of better than 2 mrad. In addition, due to the very small angular spread of the beam, a possible deviation from the nominal position along z would simply be translated into an apparent shift along x .

To identify clean single-track events, a number of quality cuts are imposed. Fake tracks, identified by an anomalously high χ^2 are eliminated. Only clean beam telescope tracks, defined as having exactly one cluster on each side of each ladder, are allowed. In addition, tracks containing beam telescope clusters with too many (≥ 6) strips or unusually low or high amplitude, indicative of a dead or noisy strip, are removed. To further suppress spurious tracks, the good collimation of the beam was exploited by doing appropriate cuts in the (m_x, x_0) - and (m_y, y_0) -planes, where m denotes the reconstructed slope of a particle track and x_0 denotes its offset. In total, we used roughly 60 000 clean single-track events for this analysis.

As an important cross-check, we reconstructed the position corresponding to each SiPM readout channel by using the beam telescope information alone and

histogramming the interpolated track position if a given SiPM channel showed an amplitude exceeding 3.5 photo-electrons. The average distance between the mean values of these histograms is then the reconstructed readout pitch. It was found to agree with the nominal value of 250 μm to within 2 μm .

5.3. Results

The key figures of merit of a complete tracker module are the spatial resolution and the tracking efficiency that it offers. These in turn depend crucially on the overall light yield, expressed as the number of primary photo-electrons (number of incident photons that triggered a Geiger discharge in one of the pixels) detected by the SiPMs, achieved for a minimum ionizing particle crossing the module perpendicularly.

With the identification of fiber clusters as outlined in the previous section, the raw cluster amplitude – expressed as the total number of fired pixels – is easily calculated. To obtain the corresponding number of photo-electrons, this value has to be corrected for saturation effects and for crosstalk. Saturation effects occur due to the limited number of SiPM pixels so that two photons will occasionally hit the same pixel. The situation is analogous to the combinatorial problem of distributing N balls into M urns, and the necessary correction is found to be [30]

$$N_{\text{p.e.}} = \frac{\log\left(1 - \frac{N_H}{N_{\text{pix}}}\right)}{\log\left(1 - \frac{1}{N_{\text{pix}}}\right)} \cdot (1 - \epsilon) \quad (6)$$

where $N_{\text{pix}} = 80$ is the number of pixels per SiPM, N_H is the number of fired pixels and $N_{\text{p.e.}}$ is the calculated number of photo-electrons. The factor $(1 - \epsilon)$ in eq. (6) accounts for crosstalk [20]. The combined probability for crosstalk was determined from the LED spectra taken during the testbeam and was typically of the order $\epsilon \sim 0.25$. The correction is applied on a per-channel basis. The distribution of the cluster amplitudes corrected for crosstalk and saturation effects is shown in figure 21 for a typical SiPM array. While the exact shape of the distribution is governed by many factors, namely the fluctuations in primary energy deposition, fluctuations in the path-length of the primary particle in the fiber ribbon, Poisson fluctuations in the number of detected photons, and the cluster definition used, its median is by definition taken to be the light yield of the fiber-SiPM compound. Figure 21 also contains the raw amplitude distribution (after pedestal subtraction) of all the strips in clusters on the same hybrid. Here, the individual photo-electron peaks are well separated, demonstrating the auto-calibration capabilities of the SiPM arrays. The small saturation bump towards high ADC counts is due to the limited dynamic range of the VA readout chips used.

For the determination of the spatial resolution, in the direction perpendicular to the fiber axes, the residuals $\Delta x \equiv x_{\text{tr}} - x_{\text{cl}}$ are calculated. x_{tr} is the intersection point of a particle as calculated using the track information – excluding, of course, the fiber layer under study – and x_{cl} is the position reconstructed in the fiber module and calculated according to eq. (5). Figure 22 shows an example of

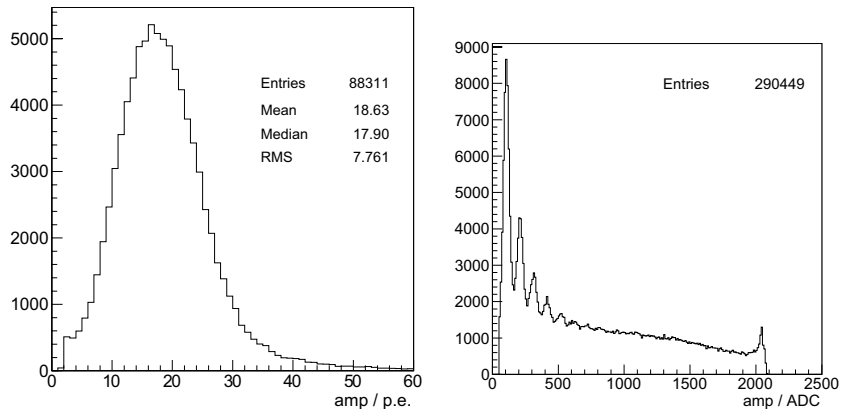


Figure 21: Distribution of cluster amplitudes, after correction for crosstalk and saturation, for a typical SiPM array (left). Distribution of individual strip amplitudes in each cluster, for the same array (right).

the distribution of residuals, for the same array as above. A simple Gaussian fit is performed and the resulting standard deviation is called the residual width.

Using the residual widths found in this way, the track fits can be redone and the χ^2 distribution for the track fit can be calculated as a crosscheck (fig. 23). Nice agreement with the theoretical expectation is found, especially if an additional outlier rejection, removing clusters with a pull of more than 4σ , is performed. Here, the residual width of the beam telescope modules in the xz -plane was assumed to be 0.025 mm. We checked that the results obtained for the spatial resolutions of the fiber modules did not depend significantly on the beam telescope resolution used in the track fit.

In order to obtain the underlying spatial resolution of the fiber-SiPM compound from the residual width shown above, the latter has to be corrected for two effects. First, multiple Coulomb scattering leads to a deviation of the particle trajectory from a straight line. Second, due to the limited resolution of the silicon beam telescope and the other fiber layers, the true track position is not perfectly known. These effects have been included in a Monte Carlo study – based on the Geant4 [19] package – which models the material budget present in the testbeam setup and the multiple scattering process and uses the same tracking techniques as the testbeam analysis, to calculate the necessary corrections.

Figure 24 contains the main result of the testbeam. Here, the light yield and spatial resolution that were achieved for the prototype modules are shown, with each data point corresponding to one silicon photomultiplier array. Different markers are used to distinguish between arrays reading out modules made from Kuraray SCSF-81MJ and SCSF-78MJ fibers, respectively, and to identify those arrays with additional optical grease in front of them. The correction for limited

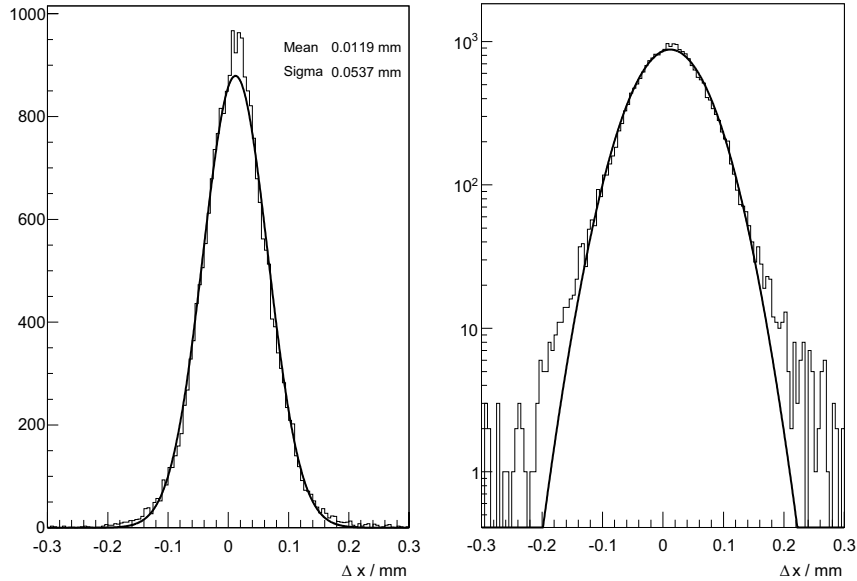


Figure 22: Track residuals for the same array as in fig. 21, in normal (left) and logarithmic (right) scale. The histogram has been fitted with a Gaussian.

track resolution and multiple scattering has been applied according to

$$\sigma_x^2 = \sigma_{\text{res}}^2 - \sigma_{\text{MC}}^2 \quad (7)$$

where σ_{res} is the residual width as shown for example in fig. 22, σ_{MC} is the root mean square deviation of the true track position from the reconstructed one as found in the Monte Carlo simulation described above, and σ_x is the underlying spatial resolution of the tracker module, plotted in fig. 24. We conservatively assumed an intrinsic resolution of 0.02 mm for the beam telescope ladders. Larger values, as indicated by the χ^2 distribution (fig. 23), would increase the necessary correction and therefore result in lower values of σ_x . A typical value is $\sigma_{\text{MC}} \cong 18 \mu\text{m}$. The error bars shown in the figure are calculated as a quadratic sum of the statistical and systematic uncertainties. The statistical uncertainties are calculated from the χ^2 variation in the Gaussian fits of the residual distributions and are typically $\lesssim 1 \mu\text{m}$, except for a few arrays that were located at the edge of the beam-spot, which leads to a lower number of contained events and thus larger statistical uncertainties. The systematic uncertainties are estimated by varying the resolution of the beam telescope ladders in the range from 0.01 mm to 0.03 mm and are $\lesssim 4 \mu\text{m}$ for the arrays with the best spatial resolution.

The results clearly show that a spatial resolution of better than 0.05 mm has been achieved for some of the prototype modules made from SCSF-78MJ fibers. At the same time, the light yield is in the range from 14 to 20 photo-electrons

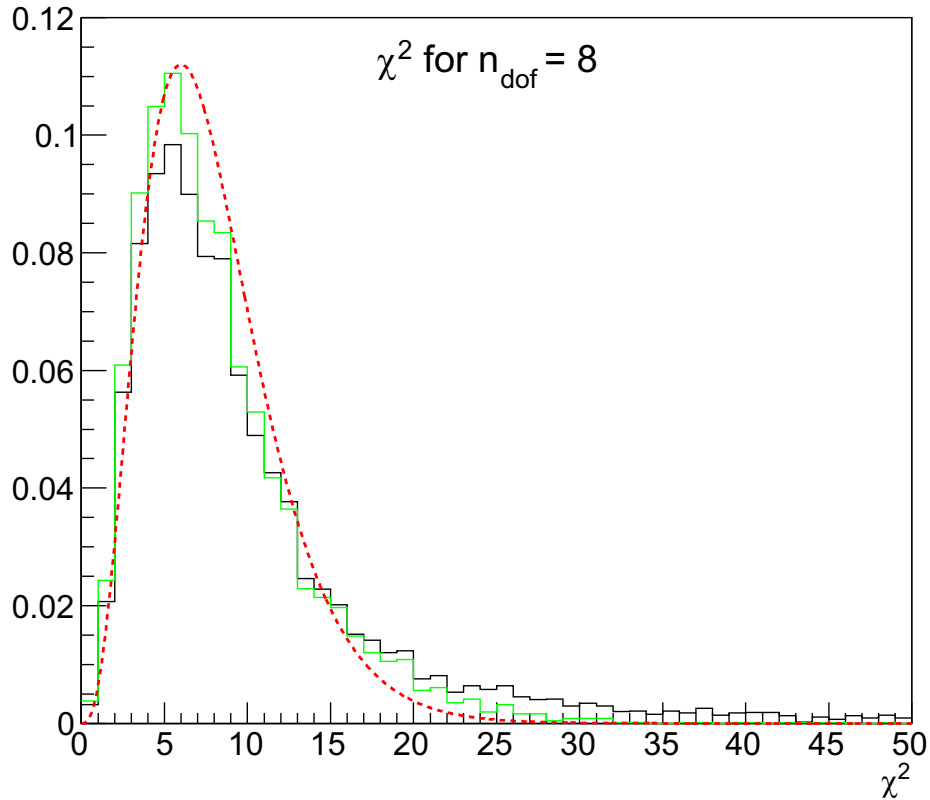


Figure 23: Normalized χ^2 distribution for tracks with $n_{\text{dof}} = 8$. The black (dark) histogram is the distribution for tracks passing all quality cuts described in the text. The green (bright) histogram is obtained if an outlier rejection is performed in addition. For comparison, the red (dashed) curve is the theoretical expectation (χ^2 distribution for eight degrees of freedom).

(corresponding to mean values of 15 to 22 photo-electrons) for most of the arrays. Despite the limited statistics available, the figure also suggests that the optical grease leads to an improved performance in terms of spatial resolution and a more homogeneous light yield. Finally, there is a clear correlation between light yield and spatial resolution, and the choice of fiber material can affect the light yield by more than a factor of two. The degradation of spatial resolution with decreasing light yield can be understood from the statistical fluctuations inherent in the calculation of the cluster position according to eq. (5).

For the high-yield fiber modules, i.e. those containing SCSF-78MJ fibers, the corresponding tracking efficiency varies between 98.5 % and 99.5 %. For the modules built with SCSF-81MJ fibers, this value is worse, on the order of 90 %.

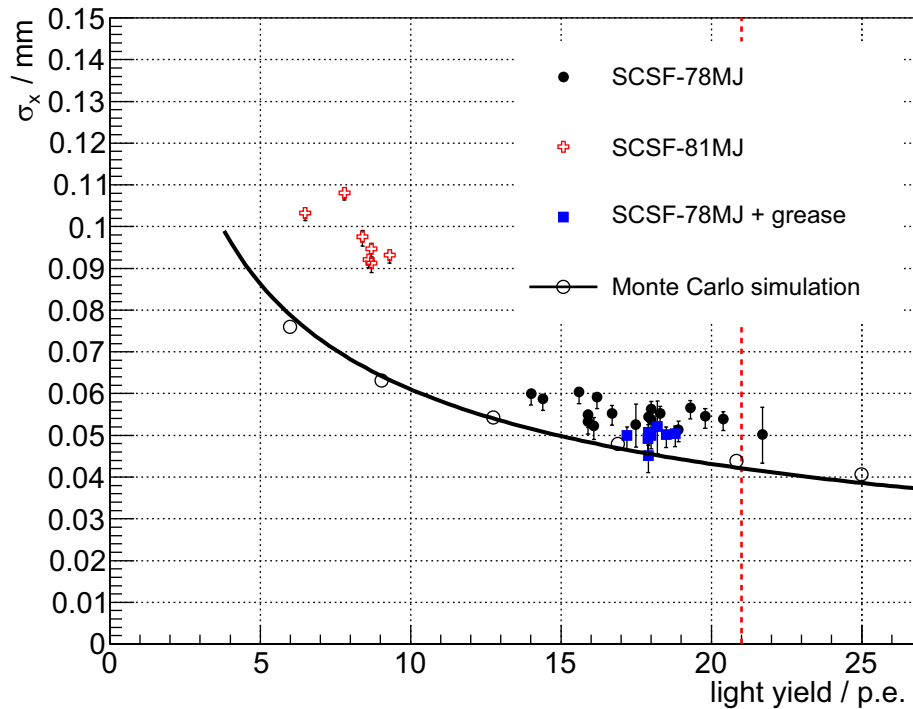


Figure 24: Achieved spatial resolution of the tracker modules as a function of the light yield. Each point corresponds to one SiPM array, using different markers for different configurations of the tracker modules, regarding the fiber type employed and the presence of optical grease for the coupling of the scintillating fibers to the SiPM. The dashed line marks the expected light yield as calculated in section 5.4. The prediction of the Monte Carlo simulation described in section 5.4 is included, along with a fit to the results of the Monte Carlo simulation according to eq. (8). The quoted light yields are the median values of the respective amplitude distributions. Taking the mean values instead would result in values that are higher by $1 \div 2$ photo-electrons.

5.4. Discussion

To compare the results obtained in the previous section to expectations, first the expected average light yield for a fiber ribbon can be estimated as follows. On average, a minimum ionizing particle (MIP) deposits 200 keV/mm in the scintillator material. From this energy deposit, 8.25 photons/MeV are generated. For the tracker geometry presented here, five layers of 0.25 mm fibers with glue gaps of 0.02 mm , the average path length of a particle for perpendicular incidence is calculated to be 0.69 mm . Therefore, a MIP creates 980 photons per fiber stack. Here and in the following, we quote the median values of the distributions in order to be less sensitive to tails in the distributions. The light trapping efficiency of the fibers is defined by the refractive indexes of the core and cladding materials and is 5.4% in each direction along the fiber axes. In total, 105 photons are trapped inside the fibers. Due to attenuation and

reflection losses in the fibers and at the mirrors at the far side of the fibers, respectively, only 68 % or 72 photons reach the readout SiPM. The fiber stack measures 1.2 mm in height while the height of the SiPM array is only 1.1 mm. In addition, the Hamamatsu SiPM arrays are protected by a glue layer of 0.275 mm thickness so that photons emitted by a fiber near the fringe of the SiPM array may be lost due to the angular emittance distribution. These two geometrical effects lead to losses of 26 %, i.e. only 53 photons reach the sensitive area of the SiPM. The photon detection efficiency at an overvoltage of 2 V is 40 % so that the expected average signal is 21 photo-electrons. This value has been marked by the dashed line in fig. 24.

We developed a Monte Carlo simulation of the detector to understand the dependence of the spatial resolution on light yield. The simulation of a passing particle starts with the generation of the primary energy deposition, based on the path length in each fiber and according to the appropriate distribution that was extracted from Geant4 [19]. The light-loss effects detailed in the previous section are taken into account to derive a mean number of photons for each fiber from which the actual number of photons to be distributed onto the SiPM array is sampled from a Poisson distribution. The response of the SiPM array is modeled taking the Geiger-mode readout, electronic noise, as well as the effects of pixel crosstalk and strip crosstalk into account. We use the appropriate probabilities as determined in laboratory measurements (fig. 17) for an overvoltage of 2 V, at which the SiPM arrays were operated during the testbeam. In addition to these effects, we expect a contribution to the detector resolution from optical crosstalk between the fibers. As a first approach, this effect is included here as an additional optical contribution to the electrical strip crosstalk probability of 3 %. The value for the optical crosstalk of 5 % is a free parameter in the Monte Carlo simulation and has been adjusted to reproduce the cluster profile properties as measured in the testbeam. Finally, fake hits are added according to the fake rate measured in the laboratory (fig. 17). To illustrate the overall good description, we compare a typical noise spectrum, the distribution of cluster length, and the average signal cluster for testbeam data and simulation in figures 25, 26, and 27, respectively. The latter represents an especially important crosscheck, as the cluster shape depends crucially on all the effects mentioned above and at the same time, it is the basis for the calculation of the particle intersection point according to eq. (5).

The prediction of the Monte Carlo simulation for the detector resolution as a function of light yield is included in figure 24. For the light yield range relevant to our study, the results for the detector resolution σ_x in the simulation can be described as

$$\sigma_x = a/\sqrt{n_{\text{pe}}} \quad (8)$$

where n_{pe} is the light yield. A fit to the simulation results for SCSF-78MJ fiber modules with optical grease yields a value of $a = 0.193$ mm. It can be seen that the prediction of the Monte Carlo simulation is too optimistic by about 0.005 mm for the high-yield modules, and the resolution of the low-yield module is underestimated by roughly 20 %, but the trend of the data is well reproduced.

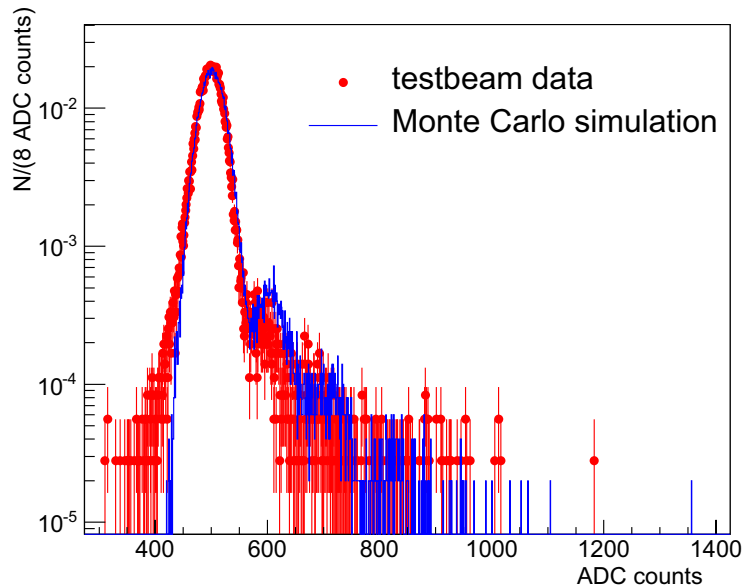


Figure 25: Noise spectrum as measured for a typical Hamamatsu SiPM array during the testbeam compared to the Monte Carlo simulation.

6. Outlook

An important issue that limits the spatial resolution achievable in the current configuration is the fact that the distribution of photons on the SiPM array is smeared out over several channels because of the optical gap between SiPM array and fiber. The photons have to bridge a distance of $275 \mu\text{m}$ defined by the optical glue that Hamamatsu puts on their MPPC 5883 SiPM devices, to protect them against environmental and handling damage. While the influence of crosstalk and the closely linked strip crosstalk as well as the total detected light yield of the fibers play a dominant role for the achieved performance of the detector module, the thickness of the glue layer on top of the SiPM devices can be modified much more easily since it does not require a complete redesign of the SiPM.

Devices with a reduced glue layer of 0.1 mm have already been delivered by Hamamatsu and should allow for a position resolution of 0.04 mm. A new generation of 64-channel SiPM arrays with no additional glue layer has been designed and will become available in summer 2010. In addition, the optical coupling has been optimized further. Both effects together should allow for a position resolution of 0.035 mm according to Monte Carlo simulations. It is also obvious that optimized software algorithms which take the discrete structure of the detector into account could lead to further significant improvements. Finally, Monte Carlo simulations show that the optimal readout pitch for a fiber detector constructed from 0.25 mm fibers would be 0.125 mm. In addition,

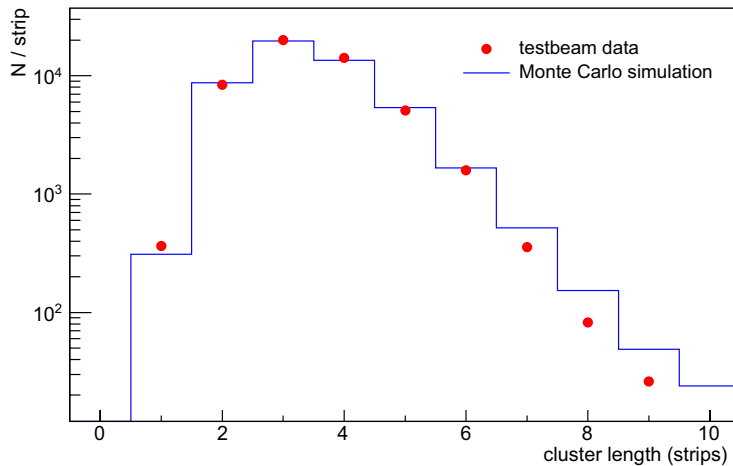


Figure 26: Distribution of cluster length (number of SiPMs in array above threshold) as obtained from testbeam data, compared to the Monte Carlo simulation.

the new 64-channel SiPM arrays would also allow a double-sided readout of the fibers. These measures together would allow the construction of scintillating fiber tracker modules with high intrinsic redundancy and an ultimate position resolution of better than 0.02 mm according to Monte Carlo simulations.

Acknowledgments

We gratefully acknowledge the generous support from R. Battiston, G. Ambrosi and P. Azzarello of the INFN Perugia who allowed us to use tracker ladders from the AMS-02 project for the beam telescope. We thank CERN for valuable beam time and support during the testbeam measurements. The measurements of the angular emission spectra were performed at the Georg Simon Ohm college in Nuremberg. The setup for the determination of the fill factor is based on an idea pioneered by H.G. Moser at the Max-Planck-Institut für Physik in Munich.

References

- [1] R.C. Ruchti, *Annu. Rev. Nucl. Part. Sci.* 46 (1996) 281-319
- [2] DØ Collaboration, *Nucl. Instr. Meth. A* 565 (2006) 463-537
- [3] M. Ellis, *Int. J. Mod. Phys. A* 20 (2005) 3815-3819
- [4] P. Annis et al., *Nucl. Instr. Meth. A* 412 (1995) 19-37
- [5] K2K Collaboration, *Nucl. Instr. Meth. A* 453 (2000) 165-176
- [6] M. Atac et al., *Nucl. Instr. Meth. A* 320 (1992) 155-160

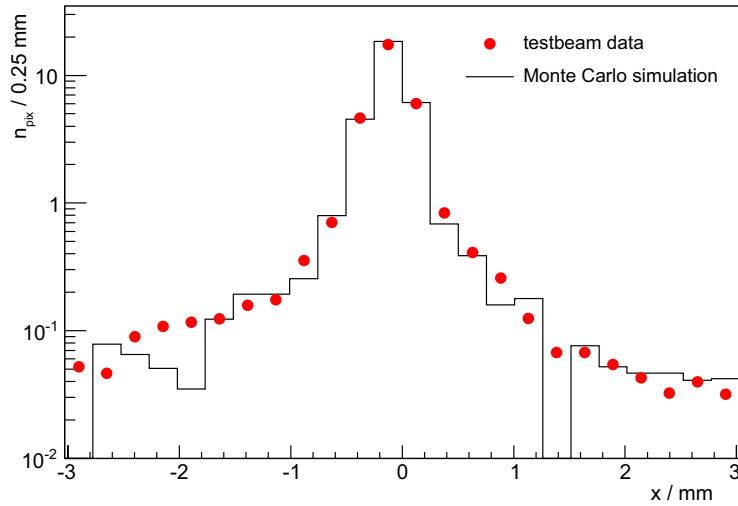


Figure 27: Average signal cluster as obtained from testbeam data, compared to the Monte Carlo simulation.

- [7] B. Dolgoshein et al., Nucl. Instr. Meth. A 563 (2006) 368-376
- [8] M. McClish et al., Nucl. Instr. Meth. A 567 (2006) 36-40
- [9] P. Buzhan et al., Nucl. Instr. Meth. A 504 (2003) 48-52
- [10] P. Buzhan et al., Nucl. Instr. Meth. A 567 (2006) 353-355
- [11] D. Renker, Nucl. Instr. Meth. A 567 (2006) 48-56
- [12] M. Danilov, Nucl. Instr. Meth. A 604 (2009) 183-189
- [13] H. Gast et al., PoS(idm2008)023
- [14] Kuraray Co., Ltd., Japan
- [15] IDEAS Integrated Detector & Electronics AS, Norway
- [16] Bitwise Systems, USA
- [17] Zumbach Electronic AG, Orpund, Switzerland
- [18] Hamamatsu Photonics K.K., Japan
- [19] S. Agostinelli et al., Nucl. Instr. Meth. A 506 (2003) 250-303
- [20] V. Balagura et al., Nucl. Instr. Meth. A 564 (2006) 590-596
- [21] P. Buzhan et al., Nucl. Instr. Meth. A (2009), doi:10.1016/j.nima.2009.05.150

- [22] H. Gast, Towards a precise measurement of the cosmic-ray positron fraction, PhD thesis, RWTH Aachen University, May 2009
- [23] J. Alcaraz et al., Nucl. Instr. Meth. A 593 (2008) 376-398
- [24] Nye Lubricants Inc., 12 Howland Road, Fairhaven, MA 02719, U.S.A.
- [25] M. Cristinziani, Search for Heavy Antimatter and Energetic Photons in Cosmic Rays with the AMS-01 Detector in Space, PhD thesis, Université de Genève, 2002
- [26] M. Bouchel et al., Nucl. Sci. Symp. Conf. Rec. (2007) Vol. 3, pp. 1857-1860, doi:10.1109/NSSMIC.2007.4436519
- [27] P. Azzarello, Tests And Production Of The AMS-02 Silicon Tracker Detectors, PhD thesis, Université de Genève, 2004
- [28] R.O. Duda and P.E. Hart, Comm. ACM 15 no. 1 (1972) 11-15
- [29] V. Blobel and C. Kleinwort, Proceedings of the Conference on Advanced Statistical Techniques in Particle Physics, Durham, March 2002, also in arXiv:hep-ex/0208021
- [30] N.L. Johnson and S. Kotz, Urn models and their application, Wiley 1977